JOURNAL OF THE AMERICAN CHEMICAL SOCIETY

Article

Spectroscopic Identification of the #-Fe / #-O Active Site in Fe-CHA Zeolite for the Low-Temperature Activation of the Methane C-H bond

Max L. Bols, Simon D. Hallaert, Benjamin E. R. Snyder, Julien Devos, Dieter Plessers, Hannah M. Rhoda, Michiel Dusselier, Robert A. Schoonheydt, Kristine Pierloot, Edward I Solomon, and Bert F. Sels

J. Am. Chem. Soc., **Just Accepted Manuscript** • DOI: 10.1021/jacs.8b05877 • Publication Date (Web): 31 Aug 2018

ACS Publications

is published by the American Chemical Society. 1155 Sixteenth Street N.W., Washington, DC 20036

Spectroscopic Identification of the α-Fe / α-O Active Site in Fe-CHA Zeolite for the Low-Temperature Activation of the Methane C-H bond

Max L. Bols[†], Simon D. Hallaert[‡], Benjamin E.R. Snyder[§], Julien Devos[†], Dieter Plessers[†], Hannah M. Rhoda[§], Michiel Dusselier[†], Robert A. Schoonheydt[*†], Kristine Pierloot[*‡], Edward I. Solomon[*§#] and Bert F. Sels[*†]

[†] Department of Microbial and Molecular Systems, Centre for Surface Chemistry and Catalysis, KU Leuven, Celestijnenlaan 200F, B-3001 Leuven, Belgium.

[‡] Department of Chemistry, KU Leuven, Celestijnenlaan 200F, B-3001 Leuven, Belgium.

[§] Department of Chemistry, Stanford University, Stanford, California 94305, United States

[#] Photon Science, SLAC National Accelerator Laboratory, 2575 Sand Hill Road, Menlo Park, California 94025, United States

ABSTRACT: The formation of single-site α-Fe in the CHA zeolite topology is demonstrated. The site is shown to be active in oxygen atom abstraction from N_2O to form a highly reactive α-O, capable of methane activation at room temperature to form methanol. The methanol product can subsequently be desorbed by on-line steaming at 200°C. For the intermediate steps of the reaction cycle, the evolution of the Fe active site is monitored by UV-Vis-NIR and Mössbauer spectroscopy. A B3LYP-DFT model of the α-Fe site in CHA is constructed and the ligand field transitions are calculated by CASPT2. The model is experimentally substantiated by the preferential formation of α-Fe over other Fe species, the requirement of paired framework aluminium and a MeOH/Fe ratio indicating a mononuclear active site. The simple CHA topology is shown to mitigate the heterogeneity of iron speciation found on other Fe-zeolites, with Fe_2O_3 being the only identifiable phase other than α-Fe formed in Fe-CHA. The α-Fe site is formed in the d6r composite building unit, which occurs frequently across synthetic and natural zeolites. Finally, through a comparison between α-Fe in Fe-CHA and Fe-*BEA, the topology's 6MR geometry is found to influence the structure, the ligand field, and consequently the spectroscopy of the α-Fe site in a predictable manner. Variations in zeolite topology can thus be used to rationally tune the active site properties.

1. Introduction

With a C-H bond dissociation energy of 105 kcal/mol at ambient conditions, methane is one of the most challenging aliphatic hydrocarbons to activate. The inert nature of the molecule coincides with the highly desirable transformation of methane from currently untapped, often small-scale and disperse sources into easily transportable platform molecules suitable for chemical synthesis.[1,2] Current processes for methane activation start by its conversion into syngas. Such processes are, however, only cost-effective on a large production scale and require harsh operating conditions rendering them unsuitable for small-scale applications.[1,3,4] Iron containing enzymes (sMMO) and iron exchanged zeolites are known to convert methane to methanol with high selectivity and exceptionally low activation barriers even below room temperature. The active site in the sMMO enzyme, identified as a binuclear Fe(IV) oxo core, is capable of selective partial methane oxidation with molecular oxygen.[5,6] The Fe-zeolite system, on the other hand, accept nitrous oxide (but not molecular oxygen) as oxidant to form an active α-O site which activates the methane C-H bond at ambient temperature and pressure.[7] The high selectivity towards methanol on Fe zeolites is presumably achieved by the high dispersion of isolated oxidation sites (α-O) and trapping of the partially oxidized product to prevent overoxidation towards thermodynamically favoured oxidation products.[8]

The α-O site responsible for this remarkable activity and its α-Fe(II) precursor were recently characterized in the Fe-*BEA zeolite, making use of a combined spectroscopic and computational study involving magnetic circular dichroism spectroscopy (MCD), Mössbauer spectroscopy, and DFT and CASPT2 calculations.[9] The α-Fe site was determined to be an extra-framework high spin (S=2) mononuclear ferrous iron hosted in the *BEA zeolite's β-six membered ring (β-6MR), adopting a square planar coordination. The positioning of framework aluminium atoms in T6/T6' positions was found to be essential for the stabilization of the α-Fe site.[10] Through abstraction of the oxygen atom from N_2O, the α-Fe site forms the reactive α-O intermediate, a mononuclear high-spin (S=2) Fe(IV)=O species with square pyramidal geometry. The exceptional reactivity of the active α-O site finds its origin in its electronic structure and its vacant *trans* axial coordination position imposed by the rigidity of the zeolite lattice.[8–10]

The MFI, and FER topologies, both containing six membered rings (6MRs), have been observed to host α-Fe sites with very similar properties and reactivity to the site characterized in

Fe-*BEA.[9,11] α-Fe sites have not yet been observed in small-pore zeolites (maximum 8MR pores) which increasingly draw attention for their attractive sorption properties, improved transition metal active site stabilization and high activity in NOx reduction.[12] In the present work we report the first experimental study demonstrating methane oxidation with Fe in the chabazite (CHA) zeolite topology, and prove its ability to stabilize similar α-sites. DFT and CASSCF/CASPT2 calculations are used to support the identification of the active site. The small-pore CHA framework has a large cavity and a straightforward unit cell, consisting of only one unique T-site. On top of this, there is an elevated density of 6MRs in its topology, rendering this zeolite a promising host material for α-sites. The 6MRs are part of the d6r composite building units which frequently occur in other zeolite framework types. To experimentally verify the importance of framework Al distribution, as hypothesised by Snyder et al.,[9,10] the effect of Al pairing on the stabilization of active sites is investigated. Finally, the influence of framework topology on the structural and spectroscopic properties of the reactive α-site is discussed.

2. **Methods**

2.1 Sample preparation

2.1.1 CHA (SSZ-13) synthesis

SSZ-13 used for the preparation of samples Fe-CHA-0.22P, ^{57}Fe-CHA-0.26P, ^{57}Fe-CHA-0.36P, ^{57}Fe-CHA-0.47P and H-CHA was prepared following the CBV720 recipe from ref. 13 with N,N,N-trimethyl-1-admantylammonium cations ($TMAda^+$) as template. A molar batch composition of $1Si:0.067Al:0.22TMAda^+:0.13Na^+:0.35OH^-:24.5H_2O$ was targeted using zeolite Y (Zeolyst international CBV720) as the Si and Al source. 28.69 g of aqueous N,N,N-trimethyladamantylammonium hydroxide (TMAdaOH) solution (25 wt%, Sachem), 5.29 g of NaOH solution (15 wt%, from >98 wt% NaOH pellets, Sigma Aldrich) and 40.58 g of deionized water (18.2 MΩ cm) was mixed in a 125 ml Teflon lined stainless steel autoclave (Parr Instruments) and homogenized. 11.25 g of the zeolite Y precursor was then added and the mixture was stirred for 2 hours at ambient conditions. The autoclave was then sealed off and oven-heated at 160 °C for 4 days under static conditions.

A second recipe, intended to produce CHA with more Al in isolated configurations (for sample ^{57}Fe-CHA-0.28U), is an adapted procedure from Di Ioro et al.[14] Isolated Al is here defined as framework Al that cannot participate in the exchange of Co^{2+} cations, whereas paired Al do exchange Co^{2+}. A molar batch composition of $1Si:0.0675Al:0.50TMAda^+:0.50OH^-:44.1H_2O$ was targeted using colloidal silica and aluminium hydroxide as Si and Al sources respectively. Specifically, 38.59 g of aqueous 1 M TMAdaOH solution (25 wt%, Sachem), 8.40 g of aqueous NaOH solution (15% wt., from >98wt% NaOH pellets, Sigma-Aldrich) and 34.85 g of deionized water (18.2 MΩ cm) was transferred to a polypropylene jar and homogenized. Then 575 mg $Al(OH)_3$ (82 wt%, Sigma-Aldrich) was added and the solution was homogenized for 15 minutes under ambient conditions. Then, 13.38 g colloidal silica (Ludox HS40, 40%, Sigma-Aldrich) was added and the mixture was stirred for another 2 hours at ambient conditions. The obtained homogeneous solution was transferred to a 125 ml Teflon lined stainless steel autoclave (Parr Instruments) and oven-heated at 160 °C for 6 days with magnetic internal stirring (1000 rotations per minute).

The structure and crystallinity of the zeolites were confirmed by X-ray powder diffraction on a high throughput STOE STADI P Combi diffractometer in transmission mode with focusing Ge(111) monochromatic X-ray inlet beams (λ = 1.5406 Å, Cu-Kα source).

Porosity is measured with a 'Micrometrics Tristar II' analysis device at 77 K (-196 °C) on calcined dried samples (6 hours at 300 °C). The relative nitrogen pressure is varied between 0.01 and 0.99. The micropore volume (ml g^{-1}) is extracted from t-plot analysis on the adsorption branch.

2.1.2 Introduction of iron

Fe-CHA materials were prepared by a strategy analogous to the samples in refs. 9–11: Fe was introduced into dried H-CHA (synthesised in the lab, section 2.1.1) by diffusion impregnation in a solution of $Fe(acac)_3$ in toluene (25 ml/g zeolite). The concentration of $Fe(acac)_3$ in toluene is approximately 0.01 M. For ^{57}Fe-CHA samples, ~100% $^{57}Fe(acac)_3$ was used in the diffusion impregnation step. All samples were calcined in air with a heating ramp of 2 °C/min to 550 °C for 30 hours to remove organic material. Samples are identified by a code of the form M(,N,O,...)-CHA-*x*P/U, in which M(,N,O,...) stands for the exchanged cation(s), *x* for the weight percentage iron in the sample and P or U indicates whether the framework aluminium atoms occur to a relatively large extent in paired configuration (P) or unpaired configuration (U), as defined by the Co^{2+} exchange capability (section 2.1.3).

2.1.3 Measurement of aluminium pairing by Co^{2+} exchange

Cobalt probing of the Al-configuration of the CHA-zeolites was performed based on methods reported for other zeolite frameworks by Dědeček and coworkers.[15] First, the H^+ or partial Na^+/H^+ form of calcined materials (after synthesis and washing) is exchanged to the Na^+-form via aqueous phase ion-exchange using 150 ml of a 0.5 M NaCl solution per gram of solid material at ambient conditions under stirring. This procedure is repeated 3 times with exchange times of at least 8 hours. After exchange the solids are collected via centrifugation and washed at least three times with deionized water (18.2 MΩ cm), (150 cm^3 per gram of solid material). Na-form zeolites are dried at 373 K under stagnant air. The same procedure is then repeated in the subsequent Co^{2+}-exchange, with a 0.05 M $Co(NO_3)_2$ solution (3x; 150 cm^3/g zeolite).

Al, Si, Co and Fe content of the resulting samples was determined by digesting the samples in concentrated HF and aqua regia followed by elemental analysis with inductively coupled plasma

(Perkin Elmer Optima 3300 DV) coupled to atomic emission spectroscopy (ICP-AES). From elemental analysis of Si, Al and Co, the absolute content of Al pairs is equated to the Co^{2+} exchange capacity and is calculated per 1000 T-atoms: [1000/(Si/Al+1)]*(Co/Al), with Si/Al and Co/Al in molar ratios.

2.2 Fe-CHA Sample treatment

Calcined Fe-CHA samples were loaded in a quartz reactor fitted with a window for *in* situ DRS-UV-Vis-NIR and a pyrex side arm for *in situ* Mössbauer measurements, allowing for spectroscopic measurements in identical conditions. A standard treatment procedure consists of an activation step in a 20 ml/min flow of He at 900 °C for 2 hours, treatment in 35% N_2O/He atmosphere for 20 min at 160 °C, and a 30 minute treatment in 30 ml/min CH_4 flow at room temperature. All flows were controlled with mass flow controllers (Brooks Instrument 0154). Flows are given for STP conditions.

2.3 Extraction and GC analysis

A known mass (~0.2 g) of dry sample was transferred into a 7 ml screw lid vial with 1 ml distilled water, 1 ml acetonitrile and a stirring rod. The mixture was allowed to stir for 24 hours (1000 rpm) at room temperature and then centrifuged. The solution was analysed on an Agilent 6850 gas chromatograph fitted with an HP1 column and a flame ionization detector (GC-FID).

2.4 Mass spectrometry

Alternatively, a steam extraction was performed after CH_4 reaction by passing a 20 ml/min stream of He saturated (at room temperature) with H_2O over the sample at 200°C. The methanol yield was quantified by integrating the m/z = 31 signal on the mass spectrum obtained by in line mass spectrometry (Omnistar Pfeiffer Vacuum GSD 30102 quadrupole mass spectrometer).

The steam desorption of methanol was described by other authors to yield a more complete product recovery from copper zeolites than a batch extraction in water or water/acetonitrile mixtures,[16] consistent with the results for Fe-CHA-0.22P (table 1). For quantitative analysis, it is therefore the preferred method. For comparison between different samples, batch extractions (section 2.3) are preferred for practical considerations and because batch extraction allows several samples to be run in parallel under identical conditions.

2.5 DR-UV-Vis-NIR spectroscopy

Diffuse reflectance spectroscopy (DRS) in the UV-Vis-NIR energy range (DRS-UV-Vis-NIR) was performed on a Varian Cary 5000 UV–Vis–NIR spectrophotometer at room temperature against a halon white reflectance standard in the 4000–40000 cm^{-1} energy range. All treatments before in situ UV-Vis-NIR spectroscopic measurements were performed in the quartz U-tube/flow cell, equipped with a window for in situ DRS-UV-Vis-NIR.

2.6 Mössbauer spectroscopy

^{57}Fe Mössbauer spectra were recorded with a See Co. W302 resonant gamma ray spectrometer in horizontal geometry at room temperaturewith zero external field using a 1.85 GBq source (Be window, Rh matrix). Data were collected from samples enriched with 100% ^{57}Fe.

Isomer shifts are given relative to α-iron foil at room temperature. Spectra were collected with 1,024 points and summed up to 512 points before analysing, and then fit to (pseudo-)Lorentzian doublets and/or sextets using the Vinda software package for Microsoft Excel.

2.7 Computational details

2.7.1 DFT geometry optimizations

Cluster models of the d6r or the 8MR cation exchange site of CHA were obtained from the crystallographic coordinates of CHA.[17] Terminal O atoms were end-capped with H and frozen during the geometry optimization, whereas H was allowed to optimize its O-H bond distance, but the direction of the bond was fixed. Then, Fe (or Fe=O) was placed in the ring and a new structure optimization was performed on the quintet surface, keeping the terminal O and H atoms fixed in position. These DFT structure optimizations were performed with Turbomole 7.1 software [18] using the B3LYP [19–24] functional, a def2-QZVPP [25] basis set on Fe and def2-TZVP [26] basis sets on all other atoms. The Cartesian coordinates of all full B3LYP-DFT optimized models in this study can be found in SI section S8.

The binding energy (BE) for Fe(II) to the cluster was calculated as follows:

$$BE = E[Fe(II)] + E[Cluster] - E[Cluster(Fe(II))] \quad (1)$$

Due to the large electrostatic attraction between the bare Fe(II) ion and the negatively charged zeolite clusters, unrealistically large binding energies are obtained from these calculations. Therefore, all discussions will be based on relative rather than absolute binding energies. The distortion of the cluster by Fe(II) was quantified by means of the strain energy (SE), which is calculated as follows

$$SE = E[\text{Distorted Cluster}] - E[\text{Cluster}] \quad (2)$$

Here, E[Distorted Cluster] is the single point energy of the optimized Fe-containing cluster where Fe is removed.

2.7.2 CASSCF/CASPT2 calculations

The ligand field (LF) spectrum of Fe(II) in the different d6r clusters was calculated using state average single point CASSCF/CASPT2 [27] calculations on the B3LYP-DFT optimized models, making use of the MOLCAS-8.1 software.[28] Extended ANO-RCC basis sets [29,30] were used, contracted to [7s6p5d3f2g1h] for Fe, [4s3p2d1f] for O, [4s3p1d] for Si and Al, and [2s1p] for H. A scalar-relativistic second order Douglass-Kroll Hamiltonian [31] was used and a Cholesky decomposition technique (with a threshold of 10^{-6} a.u.) was used to approximate the two-electron repulsion integrals.

CASSCF/CASPT2 calculations are performed in two steps. First, a CASSCF (complete active space SCF) reference wave function is built. The active space used to construct this reference wave function was chosen according to the standard rules for transition metal complexes, [32–36] i.e. five 3d and five 4d orbitals of Fe and the bonding 2p orbitals of the coordinating O atoms. This results in 8 electrons distributed over 11 orbitals CAS(8,11). Pictures of the active orbitals are shown in figure S4 for the $R1_{OPPOSITE}$ model.

In the second step, a CASPT2 calculation is performed on the CASSCF reference wave function in order to account for the dynamical correlation contribution. In this step, all electrons except those from 1s, 2s, 2p of Fe, Si and Al and 1s of O were correlated. All CASPT2 calculations were performed with a zeroth-order Hamiltonian with the standard IPEA shift [37] and an imaginary shift [38] of 0.1 a.u.

2.7.3 Mössbauer calculations

Isomer shifts were calculated with the ORCA computational package using the B3LYP functional. The CP(PPP) basis set [39] was used on Fe, with 6-311G* on coordinating O atoms and 6-31G* on all others. A calibration curve was generated by relating the DFT-calculated electron densities at the iron nucleus ($|\psi_0|^2$) to the experimental isomer shifts for a test set of 23 structurally defined Fe complexes. The IS values of the α-Fe models were then estimated from the value of $|\psi_0|^2$ calculated for each cluster model.

Quadrupole splittings were calculated using the B3LYP functional, with TZVP on Fe and coordinating O atoms, and 6-31G* on all others.

3. Results and analysis

Figure 1 gives an overview of the samples featured in this study. Similar Si/Al ratios of ~10 were obtained for all samples by ICP-AES analysis and a clear difference in Al pair density between the ^{57}Fe-CHA-0.47P (paired Al) and ^{57}Fe-CHA-0.28U (unpaired Al) (*cfr*. Methods section 2.1.2 for sample naming) samples is evident from the Co^{2+} exchange capacity (*cfr*. Methods section 2.1.3) of the protonated parent zeolites (H-CHA). Co^{2+} is herein assumed to fully and exclusively occupy exchange positions provided by Al pairs, as described in ref. 15. Fe/Al ratios and Fe weight percentages vary from sample to sample, ranging between 0.029 - 0.048 and 0.22 wt% - 0.47 wt% respectively. For ^{57}Fe-CHA-0.47P and ^{57}Fe-CHA-0.28U, microporosity was determined by N_2 physisorption to be 0.32 cm³/g. Crystallinity of the samples was confirmed by XRD. Diffractograms can be found in supplementary information section S1.

	Fe-CHA-0.22P	^{57}Fe-CHA-0.26P	^{57}Fe-CHA-0.47P	^{57}Fe-CHA-0.28U	H-CHA
Si/Al	10.1	12.5	8.5	9.4	8.6
Fe (wt%)	0.22	0.26	0.47	0.28	/
Fe/Al	0.029	0.038	0.048	0.031	/
MeOH (µmol/g)	26.8[a]; 21.3	/	14.3	4	1
MeOH/Fe (mol_{MeOH}/mol_{Fe})	0.681[a]	/	0.169	0.079	/
Al pairs per 1000 T-atoms[b]	/	/	9.0	5.1	/

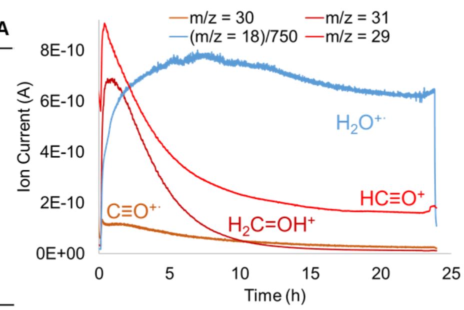

Figure 1: Left: Elemental composition and aluminium pairing of the samples and methanol yields from extraction and steaming. Right: Mass spectrum of the reactor outflow during the course of steam desorption from Fe-CHA-0.22P after methane reaction. Three distinct MeOH ionization fragments (*m/z* = 29; 30; 31) and the signal for H_2O (*m/z* = 18), scaled by a factor 750 are measured. [a] MeOH yield as obtained by steam desorption and MS analysis, all other yields are obtained by batch extraction and GC analysis; [b] Al pairs were quantified on the parent H-CHA samples. P refers to paired, U to unpaired (*cfr*. section 2.1.2).

3.1 Conversion of methane to methanol over Fe-CHA

After a full treatment cycle, consisting of activation in He at 900 °C, N_2O reaction at 160 °C and reaction with CH_4 at room temperature, a product desorption from Fe-CHA-0.22P was performed by passing a flow of steam saturated He over the zeolite at 200 °C. The outflow was followed by on-line mass spectrometry and the amount of methanol desorbed was recorded (figure 1). In accordance with the steam desorption of methanol from copper zeolites,[16,40] methanol desorption (*m/z* = 30 and 31) coincides with the breakthrough of water (*m/z* = 18). CO_2 (*m/z* = 44) was also followed, but the signal was indiscernible from the baseline. Methanol desorption is only complete after several hours in these conditions and the flow of desorbing methanol gradually decreases. The methanol desorption amounts to a molar extracted methanol to Fe ratio of 0.68.

This ratio exceeds 1:2 and indicates that, assuming a stoichiometric reaction, every active site is, at least on average, composed of less than two iron atoms.

3.2 DRS-UV-Vis-NIR study of the active iron sites

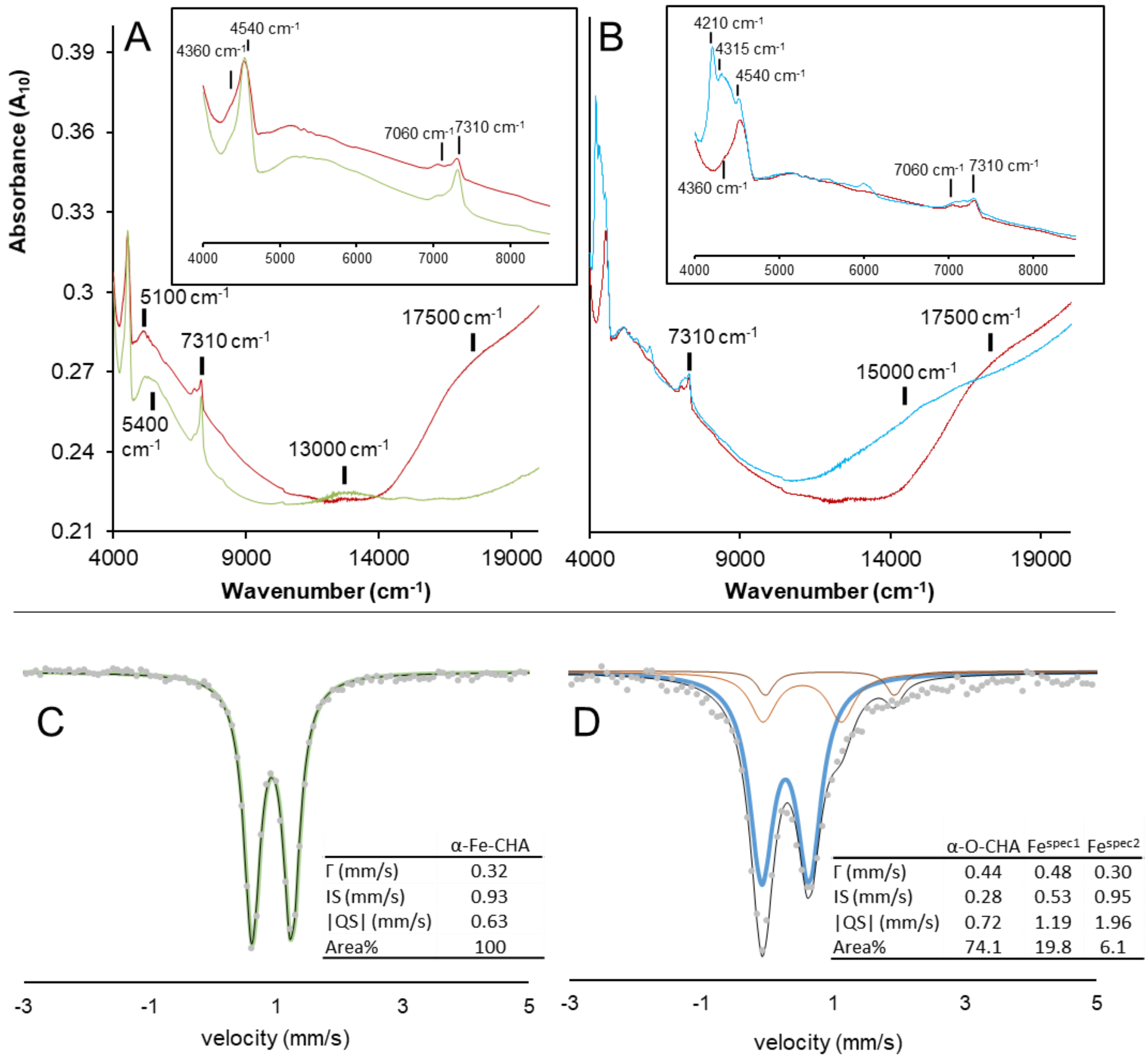

Figure 2: DR-UV-Vis-NIR spectra of Fe-CHA-0.22P (top) and Mössbauer spectra of ^{57}Fe-CHA-0.26P (bottom). A) the green spectrum is measured after He treatment at 900 °C, the red spectrum is measured after subsequent reaction in N_2O atmosphere at 160 °C. B) the red spectrum is the same as the red spectrum in A, the blue spectrum is measured after subsequent reaction with CH_4 at room temperature. Enlarged figures of the 4000 – 8500 cm^{-1} regions are given in the insets. C) room temperature Mössbauer spectrum of ^{57}Fe-CHA-0.26P after He treatment at 900 °C, the green spectrum is the α-Fe component of the fit. D) after subsequent N_2O reaction at 160 °C, the fitted spectrum is shown in black, the blue spectrum is the α-O component of the fit, the brown doublets are the components attributed to spectator Fe.

Figure 2A (and figure S8 for the full range spectra) shows the DRS-UV-Vis-NIR spectra obtained after He treatment and subsequent N_2O activation of Fe-CHA-0.22P. The relatively sharp bands at 7310 and 7060 cm^{-1}, observed in the NIR range of the spectra of of Fe-CHA-0.22P and H-CHA (figure S6), are the overtones of OH stretching vibrations of respectively silanol groups and bridging hydroxyls.[41–43] Bands at 4540 cm^{-1} and 4360 cm^{-1} are the $\nu_1+\delta_1$ combination bands of the silanol and bridging hydroxyl groups.[44]

The broad bands of Fe-CHA-0.22P at 5400 cm^{-1} (5000-6500 cm^{-1} range) and 13000 cm^{-1}, observed after He treatment at 900 °C are ascribed to ligand field (LF) transitions of Fe^{2+}, as these bands are absent in H-CHA. Upon N_2O activation, the 13000 cm^{-1} band disappears and the 5400 cm^{-1} band loses intensity on its high energy side. As a consequence its maximum shifts to 5100 cm^{-1}. This is indicative for the presence of two Fe species with d-d transitions in the ~5000 cm^{-1} region: one with d-d transitions at 13000 and 5400 cm^{-1} and one with a d-d transition in the 5100 cm^{-1} range, the latter appearing during the N_2O reaction step. New bands appear with maxima around 17500, 27000 and 37000 cm^{-1} which can be attributed to a newly formed Fe site upon heating in N_2O. After reaction with CH_4 at room temperature (figures 2B ans S8), these bands all disappear, indicating an interaction of the newly formed Fe site with methane, and new bands appear around 15000 cm^{-1} and 32000 cm^{-1}. In addition, sharp, new vibrational features appear at 4210 and 4315 cm^{-1}. These bands, also present in the system H-CHA + CH_4, are attributed to combination bands of methane vibrations. The bands at 17500, 27000 and 37000 cm^{-1} after heating in N_2O and the bands at 15000 and 32000 cm^{-1} after CH_4 reaction are also weakly present in H-CHA (figures S6 and S7). This is consistent with the methanol extraction yield of 1 µmol/g on this material and is attributed to minor iron impurities in the zeolite synthesis.

3.3 Mössbauer spectroscopy of the α-Fe-CHA and α-O-CHA sites

The sample ^{57}Fe-CHA-0.26P was prepared with isotopically labelled $^{57}Fe(acac)_3$ for Mössbauer experiments. UV-Vis-NIR spectra of ^{57}Fe-CHA-0.26P, subjected to the same reaction cycle (*vide supra*), are highly similar to those of Fe-CHA-0.22P and can be found in the SI (figure S9). The room temperature Mössbauer spectrum of ^{57}Fe-CHA-0.26P after autoreduction in He at 900 °C (figure 2C, full range spectrum in figure S10) is closely fitted by a single lorentzian doublet with an isomer shift (IS) of 0.93 mm/s and a quadrupole splitting (|QS|) of 0.63 mm/s, indicating the presence of a single Fe^{2+} site. It is therefore concluded that the precursor to the active site for low temperature methane activation is preferentially formed under these conditions and that the features observed in the UV-Vis-NIR electronic spectra after He at 900 °C of both ^{57}Fe-CHA-0.26P (figure S9) and Fe-CHA-0.22P (figure 2A) should all be attributed to this single Fe^{2+} species. Moreover the IS and |QS| parameters are characteristic for high spin (S=2) square planar Fe(II) and are highly similar to those of the α-Fe site identified in Fe-*BEA (IS=0.89 mm/s; |QS|=0.55 mm/s).[9] The Fe^{2+} site in CHA shall therefore be referred to as α-Fe-CHA.

After oxidizing with N_2O at 160 °C, the previous Mössbauer doublet (IS=0.93 mm/s, |QS|=0.63 mm/s) is fully converted to a new Mössbauer spectrum that requires three doublets (figure 2D, full range spectrum in figure S10). A majority species (IS=0.28 mm/s, |QS|=0.72 mm/s) associated with 74.1% of the total iron content exists among two minority species associated with 19.8% (IS=0.53 mm/s, |QS|=1.19 mm/s) and 6.1% (IS=0.95 mm/s, |QS|=1.96 mm/s) of the total iron content. The majority species' parameters (IS=0.28 mm/s, |QS|=0.72 mm/s) are highly similar to those of α-O in Fe-*BEA (IS=0.30 mm/s, |QS|=0.50 mm/s),[9] indicating that 74.1% of Fe^{2+} is converted to the α-O-CHA site. When the MeOH to Fe^{2+} ratio of 0.681 obtained after a single stoichiometric reaction cycle (figure 1) is corrected for the observation that only 74.1% of Fe^{2+} is converted to α-O-CHA, the MeOH to α-Fe ratio is 0.96 or, within experimental accuracy, unity. We thus conclude that the active site for CH_4 conversion is a single, mononuclear Fe^{2+} site, as in Fe-*BEA. The Mössbauer parameters of the minority iron species Fe^{spec1} and Fe^{spec2} are consistent with respectively Fe(III) and Fe(II) species, possibly from active site deactivation by moisture and/or other impurities and side reactions. The latter Fe(II) spectator is most likely also linked to the 5100 cm^{-1} absorption feature.

3.4 Influence of aluminium distribution on the formation of α-sites

In the following results, the requirement of paired Al T-atoms (defined by the capability of exchanging $Co^{2+}(H_2O)_6$, *cfr.* Di Iorio et al. [45]) to form the α-Fe-CHA site is assessed. To this purpose, two Fe-CHA samples were prepared with similar Si/Al ratios but different degrees of Al pairing (figure 1) as defined and assessed by the exchange capacity of Co^{2+} (*cfr.* sections 2.1.1 and 2.1.3). The first sample, ^{57}Fe-CHA-0.28U, was prepared from a H-CHA material with little Al pairing (5.1 Al pairs per 1000 T-atoms). The second sample, ^{57}Fe-CHA-0.47P, was prepared from a H-CHA material with elevated Al pairing (9.0 Al pairs per 1000 T-atoms). Relatively large loadings of iron were introduced to rule out an incomplete occupation of accessible exchange sites.

Despite the identical methods of iron introduction used for both samples, and despite the similar Si/Al ratios of ^{57}Fe-CHA-0.28U and ^{57}Fe-CHA-0.47P, only half the amount of iron (0.28 wt% Fe) remains in ^{57}Fe-CHA-0.28U after impregnation and washing in toluene when compared to ^{57}Fe-CHA-0.47P (0.47 wt% Fe). This is a direct demonstration of the need for nearby Al-substituted T-sites (pairs) to coordinate multivalent cationic species to the zeolite and indicates that this plays a role in retaining Fe^{3+} during impregnation. Consequently, the impregnation can, at least in part, be seen as an ion exchange in organic solvent of the Brönsted acid protons (Z-OH) of H-CHA for the Fe^{3+} ion of the $Fe(acac)_3$ organic salt:

$$\mathrm{Fe(acac)_3} + x\ \mathrm{Z\text{-}OH} \rightarrow x\ \mathrm{Hacac} + \mathrm{Z\text{-}O}_x\mathrm{\text{-}Fe(acac)}_{3\text{-}x}$$

The room temperature Mössbauer spectra of ^{57}Fe-CHA-0.47P (figure 3B) and ^{57}Fe-CHA-0.28U (figure 3C) after He treatment at 900 °C both contain a doublet which matches the doublet parameters identified for α-Fe-CHA (figure 2C). In ^{57}Fe-CHA-0.28U the doublet represents 22.2% of iron (or 0.06 sample wt%) and in ^{57}Fe-CHA-0.28P the doublet represents 47.9% of iron (or 0.23 sample wt%). Thus more α-Fe-CHA is formed in the paired Al sample (P) than in the unpaired Al sample (U). In addition to the doublet, both Mössbauer spectra contain a six line pattern with relative peak intensities of 3:2:1:1:2:3. This originates from the splitting of the ^{57}Fe nuclear energy levels in a magnetic field. In this case, no external magnetic field is present, and the magnetic field most likely arises from the ferromagnetic properties of iron oxide (Fe_2O_3) particles which are formed at higher Fe loadings. The sextet is best fitted with parameters IS=0.37 mm/s, QS=-0.21 mm/s and an effective magnetic field B_{eff}=52 T. This corresponds to the features known for hematite.[46] Especially in the ^{57}Fe-CHA-0.47P sample, the sextet lines are asymmetrically broadened, which can either be attributed to the presence of other Fe_2O_3 phases (e.g. maghemite) or to heterogeneity in the Fe_2O_3 nanoparticle size and density. Other iron species are not distinguishable in the room temperature Mössbauer spectra, indicating that, besides the presence of Fe_2O_3, only α-Fe-CHA is stabilized at exchange sites after He treatment at 900 °C and that only paired Al allows such α-Fe-CHA site to be formed. For both samples the fit can be slightly improved by incorporating another doublet with IS = 0.64 mm/s and |QS| = 2.59 mm/s. However, this doublet overlaps both with the inner lines of the sextet and with the α-Fe-CHA doublet and cannot be clearly distinguished. Its intensity is therefore treated as a contribution to the total Mössbauer intensity, but it is not identified as an additional iron species.

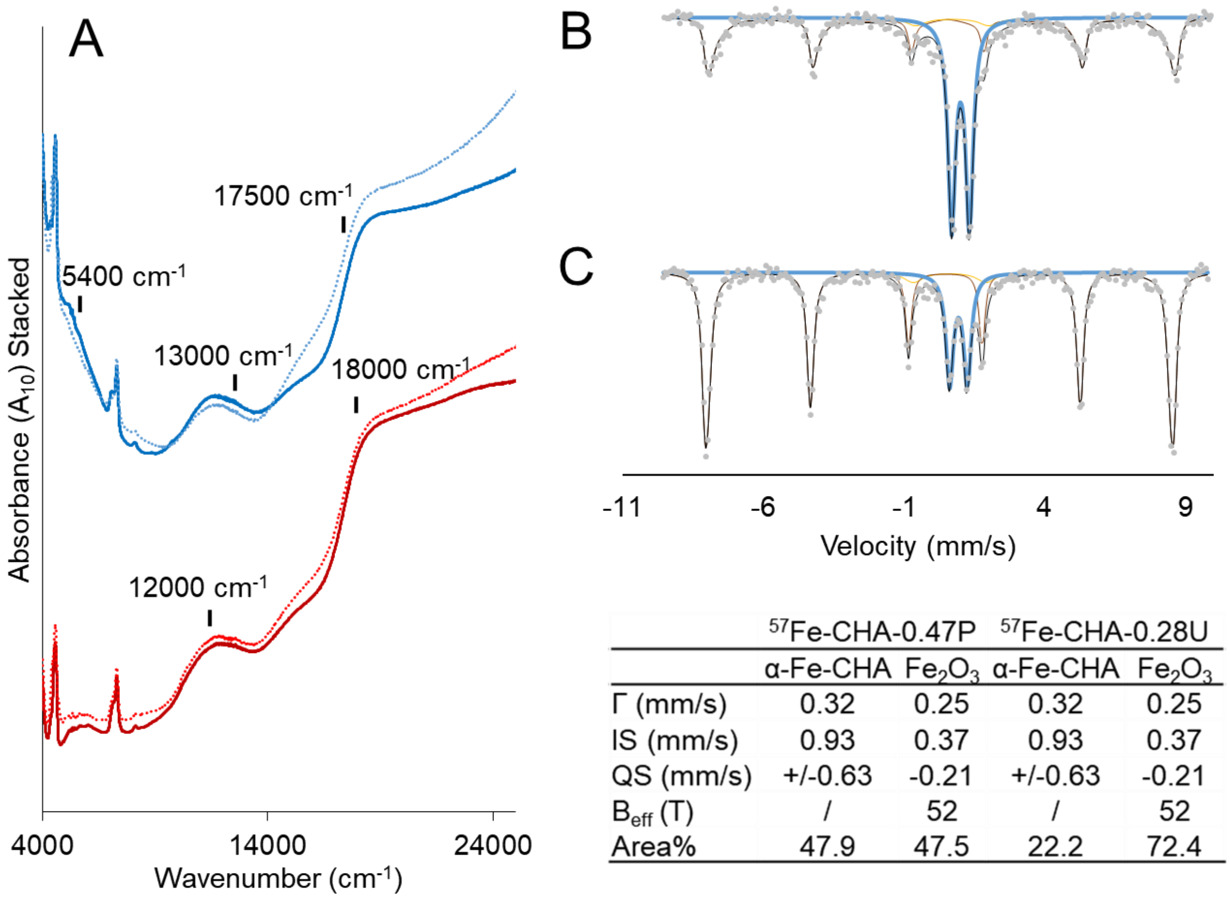

	^{57}Fe-CHA-0.47P		^{57}Fe-CHA-0.28U	
	α-Fe-CHA	Fe_2O_3	α-Fe-CHA	Fe_2O_3
Γ (mm/s)	0.32	0.25	0.32	0.25
IS (mm/s)	0.93	0.37	0.93	0.37
QS (mm/s)	+/-0.63	-0.21	+/-0.63	-0.21
B_{eff} (T)	/	52	/	52
Area%	47.9	47.5	22.2	72.4

Figure 3: A) DR-UV-Vis-NIR spectra of ^{57}Fe-CHA-0.47P (blue, top) and ^{57}Fe-CHA-0.28U (red, bottom) after He treatment at 900 °C (full lines) and after subsequent N_2O reaction at 160 °C (dashed lines). B) room temperature Mössbauer spectrum and fit of ^{57}Fe-CHA-0.47P after He treatment at 900 °C. C) room temperature Mössbauer spectrum and fit of ^{57}Fe-CHA-0.28U after He treatment at 900 °C.

The UV-Vis-NIR spectra of ^{57}Fe-CHA-0.47P and ^{57}Fe-CHA-0.28U were recorded at each step of the He, N_2O, CH_4 reaction cycle. The UV-Vis-NIR absorption spectra after the He step, forming α-Fe, and after the N_2O step, forming α-O, are overlaid to visualize the changes occurring upon N_2O activation (figure 3A). In the ^{57}Fe-CHA-0.28U spectra, a very weak feature at 17500 cm^{-1} grows in with N_2O activation but the dissipation of the 13000 cm^{-1} band (*cfr*. figure 2A) cannot be clearly distinguished. Present in both spectra (before and after N_2O) are the sharp slope at 18000 cm^{-1} and a broad band at ~12000 cm^{-1}. These do not change with N_2O treatment and are therefore not related to the active site. The absorption features at 18000 cm^{-1} and ~12000 cm^{-1} in the electronic spectra, as well as the red colour of the samples, can be attributed to the presence of Fe_2O_3, in accordance with the results from Mössbauer spectroscopy.[47,48] In the ^{57}Fe-CHA-0.47P spectra, the reduced absorption at 13000 cm^{-1} and the increased absorption at 17500 cm^{-1} upon

N_2O treatment are more pronounced. In addition, the 5400 cm^{-1} absorption linked to the α-sites in Fe-CHA is clearly present. Features of Fe_2O_3 at 18000 cm^{-1} and ~12000 cm^{-1} are present as well and these remain after reaction with N_2O. Also in the CH_4 activation step, the Fe_2O_3 features remain unchanged. The Fe_2O_3 particles therefore do not actively participate in the stoichiometric reaction with N_2O and CH_4 (figures 3 and S11).

Methanol extraction after CH_4 reaction at room temperature in H_2O/CH_3CN yields 14.29 µmol/g for ^{57}Fe-CHA-0.47P and 3.97 µmol/g for ^{57}Fe-CHA-0.28U (figure 1). From Mössbauer, 36.9% of Fe is present as α-O-CHA after N_2O reaction on ^{57}Fe-CHA-0.47P *versus* 17.3% on ^{57}Fe-CHA-0.28U (figure S12), resulting respectively in a maximum methanol yield of 31.1 µmol/g and 8.7 µmol/g (assuming MeOH/α-O = 1).

3.5 Computational modelling of the α-Fe-CHA and α-O-CHA sites

The spectroscopic evidence for α-Fe-CHA and α-O-CHA as well as the MeOH to α-O-CHA ratio ≈ 1 (α-O-CHA quantified by ICP-AES and Mössbauer and MeOH quantified by steam desorption and in line MS) support a single Fe^{2+} site as the active site. Furthermore, given that α-sites are stabilized exclusively in topologies with β-type 6MRs (*BEA, MFI, FER)[9], we place the cation in the exchange site formed by the double six membered ring (d6r) in the CHA topology.

Table 1: Strain and binding energy and the number and types of coordinated O ligands of the five optimized B3LYP-DFT cluster models with the two Al substitutions in all five possible conformations for α-Fe-CHA in the d6r. The corresponding B3LYP-DFT optimized cluster models are depicted below the table. End-capping hydroxyl groups are omitted for clarity. Colour scheme: orange = Fe, red = O, grey = Si, light brown = Al.

α-Fe-CHA DFT optimized models	Fe coordination	Binding energy (kcal/mol)	Zeolite lattice strain (kcal/mol)
$1R_{NEAR}$	$3_{Si}O_{Al}$	565.57	58.34
$1R_{OPPOSITE}$	$4_{Si}O_{Al}$	568.90	58.60
$2R_{NEAR}$	$5_{Si}O_{Al}$	536.90	61.81
$2R_{MEDIUM}$	$2_{Si}O_{Al};1_{Si}O_{Si}$	540.12	53.88
$2R_{FAR}$	$2_{Si}O_{Al};1_{Si}O_{Si}$	534.89	54.78

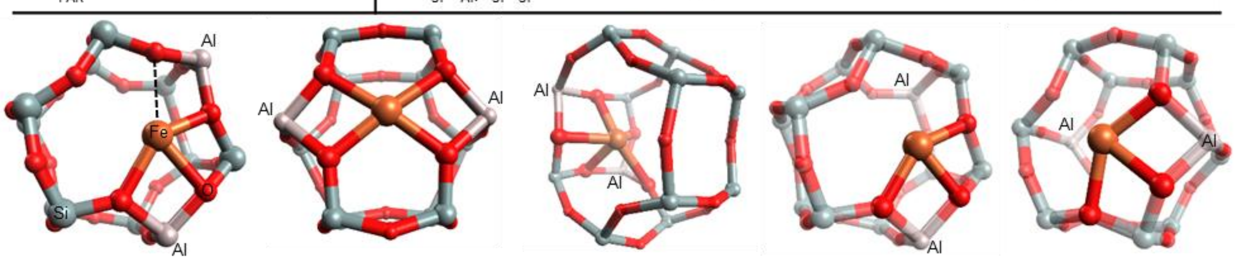

$1R_{NEAR}$ $1R_{OPPOSITE}$ $2R_{NEAR}$ $2R_{MEDIUM}$ $2R_{FAR}$

To back up this hypothesis, models with Fe(II) in the 8MR exchange site were also geometry optimised and evaluated for consistency with the experimental observations. The need for nearby framework Al T-sites was established in section 3.4, and the model d6r and 8MR exchange sites are therefore constructed to include two Al T-sites. Taking into account Löwenstein's rule, five distinct d6r models and three 8MR models can be identified with different relative positions of the aluminium tetrahedra (table 1 and figure S3). All 8MR models can, however, be excluded based on the mismatch of the calculated Mössbauer IS and QS values versus experiment (see SI section S2.1). Of the d6r models, two have both Al atoms in a single 6MR, either separated by two Si T-atoms ($1R_{OPPOSITE}$ model) or separated by only one Si T-atom ($1R_{NEAR}$ model). The other three models have one Al T-atom per 6MR, and these can be situated at nearest positions ($2R_{NEAR}$ model), at medium separation ($2R_{MEDIUM}$ model), or as far as possible ($2R_{FAR}$ model). The five exchange sites were optimized with B3LYP-DFT before and after the introduction of a single Fe(II) cation. The strongest binding energy (BE) = 569 kcal/mol is calculated for Fe(II) in the $1R_{OPPOSITE}$ exchange site, where the Fe(II) cation ligates to four framework oxygen atoms bound to an Al T-atom (${}_{Si}O_{Al}$) and adopts a square planar coordination. The second most stable structure is formed in $1R_{NEAR}$ with BE=566 kcal/mol. Here too, Fe(II) prefers to coordinate ${}_{Si}O_{Al}$ atoms, but the coordination is severely distorted. The three structures where Al is distributed over the two 6MRs are significantly less stable (BE ≤ 540 kcal/mol). The calculated strain energies (SE) and the number of coordinating ${}_{Si}O_{Al}$ ligands of the different models, presented in table 1, show that the strain on the zeolite lattice is larger when Fe(II) is coordinated with more ${}_{Si}O_{Al}$ atoms. As these ${}_{Si}O_{Al}$ are more electron donating than ${}_{Si}O_{Si}$, they interact more strongly with Fe(II), thereby causing a stronger deformation of the d6r. However, despite the larger strain in models $1R_{OPPOSITE}$ and $1R_{NEAR}$, Fe(II) is still most strongly bound at these sites.

Because the active α-Fe-CHA site is preferentially formed at low loadings (section 3.3), the most stable $1R_{OPPOSITE}$ structure is the most likely candidate for α-Fe-CHA. Similar to the α-Fe sites in *BEA, MFI and FER[9,11], this is a square planar Fe(II) site coordinated to ${}_{Si}O_{Al}$ with Al on opposite sides of a single 6MR. At higher iron loadings, only Fe_2O_3 is observed besides α-Fe-CHA (figure 3). This contrasts with Fe-MFI and Fe-*BEA, where DR-UV-Vis and Mössbauer indicate the presence of other spectator Fe species in absence of Fe_2O_3 at elevated loadings (respectively 1.0 wt% for Fe-*BEA[9] and 0.59 wt% for Fe-MFI[11]) Given the low frequency of Al-O-Si-O-Al sequences in high-silica CHA,[14,15] $1R_{NEAR}$ and $2R_{NEAR}$ are unlikely to occur. The absence of

$2R_{MEDIUM}$ and $2R_{FAR}$ however, requires further investigation. The following three hypotheses can be envisioned; 1) iron in these sites is preferentially incorporated into Fe_2O_3, 2) in the synthesized

Table 2: Experimental spectroscopic properties of α-Fe-CHA and α-O-CHA and the corresponding results from the modelled α-Fe-CHA clusters $1R_{NEAR}$ and $1R_{OPPOSITE}$ and the α-O-CHA model. Theoretical electronic transition energies and oscillator strengths were obtained at the CASPT2 level of theory. Mössbauer parameters were obtained as outlined in section 2.7.3.

		Absorption features (cm^{-1})				IS (mm/s)	QS (mm/s)
		d_{z^2}-$d_{x^2-y^2}$ energy (cm^{-1}) (o.s.)	d_{z^2}-d_{xy} energy (cm^{-1}) (o.s.)	d_{z^2}-d_{xz} energy (cm^{-1}) (o.s.)	d_{z^2}-d_{yz} energy (cm^{-1}) (o.s.)		
Experiment α-Fe-CHA		13000	5400	/	/	0.93	+/-0.63
Model α-Fe-CHA	$1R_{NEAR}$	10584 ($5.6x10^{-6}$)	6249 ($7.4x10^{-7}$)	2730 ($3.5x10^{-7}$)	800 ($1.9x10^{-7}$)	0.89	-1.41
	$1R_{OPPOSITE}$	13482 ($1.7x10^{-7}$)	4070 ($1.1x10^{-7}$)	2566 ($1.1x10^{-8}$)	1239 ($3.5x10^{-8}$)	0.84	-1.25
Experiment α-O-CHA		17500 ; 27000 ; 37000				0.28	+/-0.72
Model α-O-CHA						0.29	0.35

CHA materials aluminium does not occur in such configurations frequently enough to be detected by its Fe binding in Mössbauer, 3) iron substitution and calcination induces isomerization of the zeolite framework to form the more stable $1R_{OPPOSITE}$. Such isomerization has been detected before.[49] Which of these hypotheses is/are valid remains to be evaluated.

To further evaluate the $1R_{OPPOSITE}$ model as a suitable representation of the α-Fe-CHA active site, the ligand field spectrum and Mössbauer parameters were calculated for the two models with Al in a single 6MR. The results are summarized in table 2. In both models the $3d^6$ Fe(II) has a quintet ground state with the $3d_{z^2}$ doubly occupied. A qualitative molecular orbital scheme of Fe(II) in a square planar oxygen environment is provided in ref. 11. Focusing on the two most prominent transitions in the electronic spectrum of α-Fe-CHA (5400 cm^{-1} and 13000 cm^{-1}), close agreement with experiment is found for the CASPT2 excitation energies of the $1R_{OPPOSITE}$ model (4065 and 13478 cm^{-1}). On the other hand, the highest energy d-d transition of the $1R_{NEAR}$ model is calculated at only 10592 cm^{-1}, which is outside of the error margin of 2000 cm^{-1} commonly accepted for CASPT2.[50,51] Moreover, the calculated Mössbauer parameters for the $1R_{OPPOSITE}$ model closely match the experimental parameters (table 2), although it is not possible to distinguish between the $1R_{OPPOSITE}$ and $1R_{NEAR}$ models solely based on the Mössbauer parameters.

Based on these results, the 5400 cm^{-1} and 13000 cm^{-1} absorption bands of α-Fe-CHA are assigned as d_{z^2}-d_{xy} and d_{z^2}-$d_{x^2-y^2}$ LF transitions respectively. The experimental spectrum is most

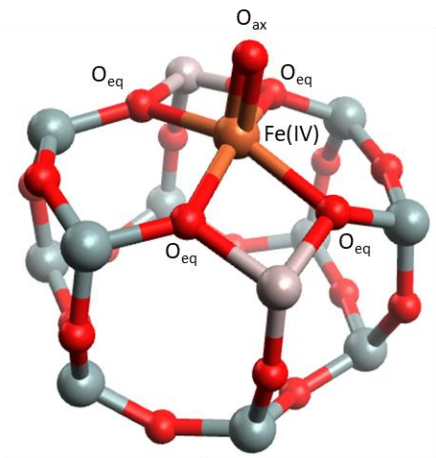

	α-O-CHA	$1R_{OPPOSITE}$
Fe=O_{ax} distance (Å)	1.60	N.A.
<Fe-O_{eq}> (Å)	2.13	2.14
Average O_{eq}-Fe-O_{eq} bite angle	87.6	89.9

Figure 4: B3LYP-DFT optimized α-O-CHA model and tabulated bond lengths of the first coordination sphere Fe ligands and O_{eq}-Fe-O_{eq} bite angles for the α-Fe-CHA and $1R_{OPPOSITE}$ models. Colour scheme: orange = Fe, red = O, grey = Si, light brown = Al.

closely reproduced by the $1R_{OPPOSITE}$ model with oppositely placed Al T-atoms in a single 6MR. This corroborates the expectations from the binding energy calculations at the B3LYP-DFT level, which showed this binding mode of iron to be the most stable. It is also consistent with the preferential formation of α-Fe-CHA over other Fe species seen experimentally (figure 2).

The α-O-CHA site was then modelled by adding an oxygen atom to the α-Fe-CHA precursor model $1R_{OPPOSITE}$ and optimizing the structure with B3LYP-DFT on the S=2 surface. The resulting structure, shown in figure 4, contains an iron(IV) in a square pyramidal coordination with an axial oxo ligand ($|Fe{=}O_{ax}|$ = 1.60 Å). Upon binding the oxo ligand, the iron atom is pulled slightly out-of-plane, as indicated by the decreased O-Fe-O bite angles. Calculated Mössbauer parameters (IS and QS) are compared to the experimental values in table 2. The calculated values for QS deviate similarly from the experimental values for α-Fe and α-O in ref. 9. The small difference between the values for |QS| of α-O found experimentally on Fe-*BEA and Fe-CHA (*vide supra*, section 3.3*)* is accurately reproduced by the difference in the calculated values from the models for α-O-*BEA (calculated |QS| = 0.24 mm/s) [9] and α-O-CHA (calculated |QS| = 0.35 mm/s).

4. Discussion

α-Fe and α-O sites had so far been confirmed spectroscopically in β-6MRs with a specific Al-O-Si-O-Si-O-Al sequence in zeolites with the FER, MFI and *BEA frameworks.[9–11] With the spectroscopic data of Fe-CHA we add a new type of 6MR as a binding site of α-Fe and α-O. This is the 6MR of the d6r building units of CHA with a similar Al-O-Si-O-Si-O-Al sequence. Notably, the d6r composite building units appear in 31 unique zeolite framework types listed on IZA, enabling the use of a wide variability of pore systems, Si/Al ratios, synthesis methods and hydrothermal properties.[17] The two Al tetrahedra must be placed at opposite sides of the same 6MR and cannot be separated over the two 6MRs of the d6r. An overview of the framework properties of relevant zeolite topologies is given in table 3. In the following paragraphs the effect of the zeolite topology on the formation and structure of α-sites is discussed.

4.1 6MR hosts for α-Fe

Two criteria are primarily considered in the selection of the host topology: the density of relevant 6MRs and the accessibility of those 6MRs. CHA has a three-dimensional pore system with diffusion restricted by 8MR windows (3.72 Å). All 6MRs occur as double six membered ring (d6MR) units which cap the CHA cages on the long ends and in fact, the entire structure can be built from connecting d6MR units (in CHA these d6MRs correspond to the d6r composite building unit).[17] This results in a much higher density of d6MR units in CHA (1.39 mmol d6MR/g) than in *BEA (0.62 mmol dβ-6MR/g) or MFI (0.70 mmol dβ-6MR/g). The d6MR units are counted as a host site for only a single α-Fe because Löwenstein's rule and the low prevalence of Al-O-Si-O-Al sequences in high-silica zeolites (Si/Al > 10) prohibit the formation of two α-Fe sites in a single d6MR.[14,15] In FER, the β-6MRs are not combined into dβ-6MRs, so here the β-6MRs are all included in the count, adding up to 0.93 mmol β-6MR/g. The CHA 6MRs are

Table 3: Topological properties of relevant zeolite topologies

	Unit cell size ($Å^3$)	Access to 6MR (Å)[a]	mmol 6MR/g	mmol β6MR/g[c]	mmol d6MR/g
CHA	2391.6	3.72 (8MR)	2.78	/	1.39
BEA polymorph A	4232.4	5.95 (12MR)	1.51	1.51	0.76
BEA polymorph B	4171.3	5.95 (12MR)	1.03	1.03	0.52
*BEA	4178.4	5.95 (12MR)	1.24	1.24	0.62
MFI	5211.3	4.70 (10MR)	5.55	1.39	0.70
FER	2051.3	4.69 (10MR)[b]	3.70	0.93	/
FAU	14428.8	7.35 (12MR)[b]	5.55	/	1.39

[a] Access to 6MR is given as the diameter of the sphere that can freely diffuse through the silicalite framework as described in ref 17. [b] The 12MR window gives access to the single 6MRs of the FAU framework. However, accessibility of the d6MR units identical to those in CHA is restricted to a 6MR window. Similarly, access to the β-6MR in FER is restricted to an 8MR window. [c] in this column, α- and γ-type 6MRs which don't host α-Fe (and don't form d6MR units) are excluded.

accessible from inside the CHA cage, which in turn is accessible through the 8MR windows. The FAU topology is also built up from d6MR motifs of nearly identical geometry and density as those in CHA. In FAU, however, they are located inside the sodalite cage and thus only accessible from the main pore system through narrow 6MR windows.[17] An overview of the relevant 6MRs and their accessibility is shown in figure S18. In addition, FAU has only been synthesised within limited Si/Al boundaries ($1 < Si/Al < 3$).[52,53] CHA, on the other hand, is stable within a wide range of Si/Al ratios ($1.15 < Si/Al < \infty$).[12,54] Its aluminium content and distribution are thus easily tuned, rendering the topology more suitable for the preparation of specific coordination environments.

Although the CHA topology has a higher concentration of suitable 6MR hosts for the α-Fe sites, not much improvement is found on the active site concentration compared to Fe-*BEA in ref. 9. From elemental analysis and Mössbauer spectroscopy, α-Fe was determined to make up 0.23 wt% of the Fe_2O_3 spectator containing ^{57}Fe-CHA-0.47P sample. Occupying all d6MRs of the CHA topology with a single α-Fe would, however, yield 7.86 wt% α-Fe. The d6MR density in CHA is therefore not the factor impeding a higher density of α-Fe sites. Analogously, from the 9.0 Al pairs per 1000 T-atoms determined on ^{57}Fe-CHA-0.47P, compensating all Al pairs with a single α-Fe site would yield 0.83 wt% α-Fe. At 0.23 wt% α-Fe, the Al pairing is therefore not the limiting factor either for the samples in this study. This study thus identifies either the selective introduction of iron into the zeolite pore system or the correct positioning of Al pairs in opposite positions of the same 6MR (i.e. in accordance with the $1R_{OPPOSITE}$ model) as limiting. Further studies should tackle the issues with achieving higher α-Fe-loadings and a higher density of suitable exchange sites. Potential strategies include modifications in the method of iron introduction, further tuning of the framework aluminium distribution for pairs to be more accessible and more accurately positioned, the screening of other 6MR containing topologies with more open pore systems, and post-synthetic modification of the CHA material to introduce mesoporosity before the iron introduction step.

Fe-CHA materials have been extensively investigated in the context of the selective catalytic reduction of NOx with ammonia (NH_4-SCR) and other $DeNO_X$ reactions.[55–58] Meanwhile, the other α-site stabilizing Fe zeolites Fe-FER, Fe-MFI and Fe-*BEA are known to be active in NH_4-SCR as well.[59] An active site, has however, not yet been unambiguously identified spectroscopically on these catalysts. By identifying the formation of square planar, high spin Fe(II) in the CHA topology, and its reliance on the presence of paired aluminium T-site substitutions, this study strongly encourages an exploration of α-Fe and α-O sites in the context of DeNOx catalysis. With the copper active site of Cu-CHA for NH_4-SCR often modelled in 6MRs with a single Al substitution,[55] the 6MR exchange sites with double Al substitution remain available for α-Fe coordination. While the copper active sites perform well for low temperature SCR, the α-Fe sites may complement the copper active sites in a mixed Cu,Fe-CHA zeolite catalyst for good performance in SCR also at high temperatures, leading to improved overall performance.

4.2 Influence of zeolite topology on the spectroscopy, geometry and binding interactions of α-Fe

α-Fe sites in Fe-CHA, Fe-*BEA, Fe-MFI and Fe-FER can be identified by two experimentally accessible d-d transitions predicted by CASPT2 calculations: d_{z^2}-$d_{x^2-y^2}$ and d_{z^2}-d_{xy}, although the latter transition is out of range in wavenumber and/or intensity to be distinguished in DRS-UV-Vis-NIR in the cases of Fe-*BEA, Fe-MFI and Fe-FER. The d-d transition energies are given in table 4 together with the Mössbauer parameters, binding energy (BE), strain energy (SE) and average Fe-O bond length (<Fe-O>) for each topology.

Similar IS and |QS| values are obtained experimentally on α-Fe in *BEA and CHA, supporting the assignment of α-Fe-CHA to a similar high-spin mononuclear square planar Fe^{2+} site. These Mössbauer parameters are characteristic for such iron species and are in agreement with Mössbauer data on other experimentally known high spin square planar Fe^{2+} complexes.[9]

Table 4: Upper rows: Ligand field spectra and Mössbauer parameters obtained experimentally and calculated with CASPT2 for α-Fe sites in CHA, *BEA, MFI and FER. CASPT2 data on *BEA (Si/Al=12.5; 0.3 wt% Fe), MFI (Si/Al=15; 0.3 wt% Fe) and FER (Si/Al=28; 0.3 wt% Fe) are taken from refs. 9 and 11. Lower rows: BE, SE and average Fe-${}_{Si}O_{Al}$ distance measured on the d6MR models on CHA and *BEA. The experimental < Fe-${}_{Si}O_{Al}$> value is taken from EXAFS data in ref. 10.

	Fe-CHA		Fe-*BEA		Fe-MFI		Fe-FER	
	experiment	$1R_{OPPOSITE}$ model	experiment	β(T6T6) model	experiment	β(T4T10) model	experiment	β(T1T1) model
d_{z^2}-$d_{x^2-y^2}$ (cm^{-1})	13000	13482	15900	16053	15200	15005	16100	17364
d_{z^2}-d_{xy} (cm^{-1})	5400	4070		4027		3613		4411
10Dq (cm^{-1})	7800	9412		12026		11392		12953
IS (mm/s)	0.93	0.84	0.89	0.72				
QS (mm/s)	+/-0.63	-1.25	+/-0.55	-0.95				
BE (kcal/mol)		568.90		606.64				
SE (kcal/mol		58.60		50.78				
<Fe-${}_{Si}O_{Al}$> (Å)		2.14	2.02	2.02				

Similar deviations from the experimental IS and |QS| are found for the computed values in table 4 for both the *BEA and CHA topologies.

Earlier calculations on Fe-*BEA, Fe-FER and Fe-MFI have shown that, even though uncommon, the square planar coordination of high spin Fe(II) is electronically preferred by Fe(II) in a suitable zeolite environment.[11] It is thus not surprising that the square planar $1R_{OPPOSITE}$ model has the highest binding energy among the evaluated B3LYP-DFT structures in table 1. As the BE and SE may vary significantly with cluster size, comparison of BE and SE of the $1R_{OPPOSITE}$ model with the smaller Fe-*BEA β(T6T6) models used in ref. 11 would be inaccurate. A larger model of the α-Fe-BEA site, d6MR β(T6T6) was therefore constructed and optimized in the same way as the other models described in this paper (figure S5). Comparing the BE of this Fe-*BEA d6MR β(T6T6) model and the Fe-CHA $1R_{OPPOSITE}$ model (table 4), we observe a larger BE in the former (ΔBE=38 kcal/mol). The higher d_{z^2}-$d_{x^2-y^2}$ transition energy observed experimentally and the stronger equatorial ligand field strength (10Dq = $E(d_{x^2-y^2}) - E(d_{xy})$) obtained from CASPT2 on models for α-Fe-BEA, α-Fe-FER and α-Fe-MFI *versus* α-Fe-CHA corroborate that α-Fe is more strongly bound in *BEA, FER and MFI than in CHA. In the corresponding models, the higher BE and the shorter Fe-O distances calculated for *BEA, MFI and FER are consistent with these observations. Lower binding energies may correlate with the mobilization of the iron cation in the presence of ligands encountered under reaction conditions (e.g. H_2O, NO, NH_3), and may influence active site deactivation through migration of the active site's metal cation and through sintering. The inverse correlation between the Fe-O distance and BE can be explained by the distortions on the 6MR required to accommodate α-Fe. These distortions are larger for the CHA 6MR than for the β-6MR of *BEA, which has a narrower 6MR in the absence of Fe (figure S13). In CHA, the average distance between trans ${}_{Si}O_{Al}$ ligands decreases upon α-Fe(II) binding by 0.761 Å (from 5.015 Å to 4.254 Å) while in *BEA this distance decreases

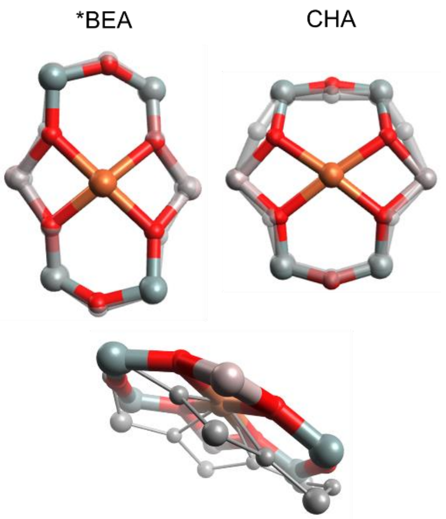

Figure 5: Above: overlays of the B3LYP-DFT optimized α-Fe models in *BEA (d6MR) (left) and CHA ($1R_{OPPOSITE}$) (right) and the corresponding B3LYP-DFT optimized models of the Al substituted 6MRs before Fe coordination. The empty 6MR models are shown in grey. Below: overlay of the Fe-CHA $1R_{OPPOSITE}$ model (coloured) and the Fe-*BEA α(T6T6) model (grey) overlapped at the α-Fe atom.

only by 0.276 Å (from 4.186 Å to 3.910 Å). Relative to the other distortions of the original CHA 6MR upon coordination of α-Fe(II), the shortening of the Fe-O bond distances appears to be the only distortion of significance (figure 5 and table S1). The lattice thus inhibits the optimal Fe-$_{Si}O_{Al}$ bond shortening in CHA and accordingly, the SE on the CHA 6MR is larger than that on the *BEA β-6MR. Consequently, as indicated by the models, the BE for α-Fe-BEA is larger than that of α-Fe-CHA because shorter Fe-$_{Si}O_{Al}$ bond lengths can be reached with a lower SE. Therefore the lower BE, the higher SE and the lower 10Dq value obtained for the 1R$_{OPPOSITE}$ model of α-Fe-CHA versus the β(T6T6) model of α-Fe-BEA are all explained by the compensating forces exerted on the Fe-$_{Si}O_{Al}$ bonds by the lattice and by the coordinating Fe(II) ion.

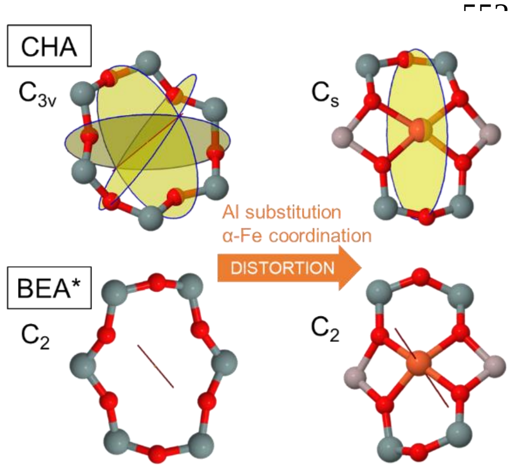

Figure 6: Point groups and symmetry elements of the 6MRs in the CHA and *BEA topologies before (from ref. 17) and after Al substitution and Fe coordination.

Despite comparable concentrations of α-Fe sites and nearly identical measurement conditions to the DRS-UV-Vis-NIR in ref. 9 (the bed of Fe-*BEA pellets is ~15% denser than the Fe-CHA bed), the 13000 cm^{-1} transition in α-Fe-CHA appears much weaker than that of the 15900 cm^{-1} transition of α-Fe-BEA. The discrepancy in absorption intensity is also reflected in the calculated oscillator strength of the d_{z^2}-$d_{x^2-y^2}$ LF transition at the CASPT2 level, which is approximately 500 times smaller for the Fe-CHA 1R$_{OPPOSITE}$ model compared to the Fe-*BEA β(T6T6) model (table S3). This observation is a consequence of the different symmetries of the two systems (figure 6). As explained in S6, the d_{z^2}-$d_{x^2-y^2}$ LF transition in C_2 symmetry (which is the symmetry point group of the Fe-*BEA β(T6T6) model) mainly gains absorbance of light polarized along the C_2 axis because of a tetrahedral twist of the coordinating O, whereas in the case of C_s symmetry (which is the symmetry point group of the Fe-CHA 1R$_{OPPOSITE}$ model) this excitation mainly gains absorbance of light polarized perpendicularly to the C_s plane through a change in opposing OFeO bite angles. As the tetrahedral twist in the Fe-*BEA β(T6T6) model is more pronounced than the change in opposing O_{eq}-Fe-O_{eq} bite angles in the 1R$_{OPPOSITE}$ model of Fe-CHA (table S2, section S5), a more intense band for α-Fe-BEA is expected.

4.3 Structural and spectroscopic comparison of the α-O sites in Fe-CHA and Fe-*BEA

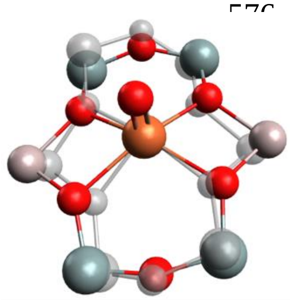

Figure 7: Overlays of the B3LYP-DFT optimized α-O-CHA (coloured) and α-O-BEA (grey) models. The models are positioned to overlap on the Fe atom and the Fe=O_{ax} bonds of the models are aligned.

Comparing the α-O site models in *BEA and CHA (figure 7), we calculate a similarly short Fe=O bond in both (1.59 Å in *BEA *versus* 1.60 Å in CHA). Adding the axial α-O onto the 1R$_{OPPOSITE}$ (Fe-CHA) and β-(T6T6) (Fe-*BEA) models pulls in the equatorial oxygen ligands by 0.1 Å only for both models, and the tetrahedral twist and difference in opposing bite angles remain similar to the α-Fe models (table S2). The Fe atom is, however, shifted out of the square plane by an additional 0.310 Å and 0.271 Å respectively in the α-O-CHA and the α-O-BEA models from its out-of-plane distance in the corresponding α-Fe models, so that the out-of-plane Fe translations are more similar between the two α-O models than they are for the two α-Fe models. All other types of distortion from square planar are increased slightly from the α-Fe models. The electronic spectrum of α-O-CHA obtained after N_2O activation (table 2) bears strong resemblance to the α-O spectrum in Fe-*BEA, where absorption bands are observed at 16900 cm^{-1}, 20100 cm^{-1} and 27000 cm^{-1}.[9] Likewise, the Mössbauer parameters of the majority species in figure 2D and listed in table 2 closely resemble those of α-O identified on Fe-*BEA.[9] Furthermore, the unique reactivity with CH_4 at room temperature is observed for the α-O sites on all of the FER, MFI, *BEA and CHA frameworks. These observations indicate that regardless of the topology, and more specifically regardless of Fe-$_{Si}O_{Al}$ bond length and symmetry distortion, the α-Fe sites form strongly reactive α-O sites upon N_2O activation on each of these zeolite topologies.

5. Conclusion

For the first time the α-Fe site, active in methane partial oxidation at room temperature after N_2O activation, is documented in the frequently occurring d6r composite building unit in the CHA zeolite topology, a zeolite industrially applied for DeNOx catalysis. The site is formed preferentially and exclusively up to at least 0.26 wt% Fe in Fe-CHA with Si/Al=12.5, with Fe_2O_3 forming the only other identifiable iron phase at more elevated iron loadings. The latter contrasts with Fe-*BEA, where other spectator Fe species are formed at high Fe loadings before Fe_2O_3 nanoparticles are found (up to ≥ 1.0 wt% for Fe-*BEA from ref. 9). The Fe-CHA α-sites have structural and reactivity properties highly similar to those identified in earlier studies on MFI, FER and *BEA, despite differences in the 6MR binding site geometries. It was shown that methanol can be extracted from the α-Fe sites by steaming at 200°C, as already established for copper zeolites, opening the door to on line cycling of the Fe zeolite material throughout the whole reaction cycle. The methanol yield from the Fe-CHA zeolites combined with Mössbauer spectroscopy indicates a 1:1 MeOH to α-O ratio which, assuming a stoichiometric reaction, confirms the mononuclearity of the active site. Also the necessity of paired framework aluminium in the zeolite 6MR, quantified by Co^{2+} titration, to stabilize the α-Fe site is confirmed experimentally. Comparison between the experimental spectroscopy and the spectroscopically validated computational models on CHA and *BEA reveals strong parallels between the α-sites with slight but informative differences. The distortion of the ligand field of the α-Fe sites from ideal square planar symmetry is shown to determine the extinction coefficient and polarization of the high energy d_{z^2}-$d_{x^2-y^2}$ transition in the electronic spectrum. Moreover, the initial diameter and symmetry of the host 6MR (C_{3v} in CHA and C_2 in *BEA) are concluded to be crucial in determining the ligand field strength and symmetry around the α-Fe site. The 6MR of CHA stabilizes a C_s symmetric α-Fe coordination which is less distorted from square planar than the C_2 symmetric α-Fe coordination in *BEA. To achieve Fe-CHA materials with improved reactivity, strategies must be developed to increase the active site density in CHA. This study indicates that improvements must be looked for at the level of the introduction of iron into the CHA pore system and/or the crystallographic positioning of Al pairs.

6. <u>Associated Content</u>

Supporting Information

XRD diffractograms, CASPT2 active space orbitals, DFT model details, additional 8MR exchange site models, additional and full range DR-UV-Vis-NIR and Mössbauer spectra, description of the 6MR symmetry in CHA and *BEA and the lattice deformations upon coordination of Fe as calculated by DFT, quantitative description of the deviations from square planar coordination of the iron site in the α-Fe models for *BEA and CHA, correlation of the d-d absorption band intensities and coordination symmetry of α-Fe, overview of the shape and accessibility of 6MRs in MFI, *BEA, FER, FAU and CHA, and Cartesian coordinates of all model structures

7. <u>Author information</u>

Corresponding Authors

*bert.sels@kuleuven.be

*kristin.pierloot@kuleuven.be

*solomone@stanford.edu

*robert.schoonheydt@kuleuven.be

8. Acknowledgements

This investigation has been supported by the Flemish Science Foundation (FWO, grants G0A2216N to B.F.S, R.A.S. and K.P. and 12E8617N to M.D.) and the National Science Foundation (grant CHE-1660611 to E.I.S.). S.D.H. and D.P. acknowledge the FWO for Ph.D. (aspirant) Fellowships. B.E.R.S. acknowledges support from the National Science Foundation Graduate Research Fellowship Program under grant DGE-11474 and from the Munger, Pollock, Reynolds, Robinson, Smith & Yoedicke Stanford Graduate Fellowship. The computational resources and services used in this work were provided by the VSC (Flemish Supercomputer Center), funded by the Hercules Foundation and the Flemish Government-department EWI. The COST Action ECOSTBio CM1305 from the European Union is also gratefully acknowledged. We acknowledge SACHEM for providing the TMAdaOH template

9. References

(1) Olah, G. A.; Goeppert, A.; Prakash, G. K. S. *Beyond Oil and Gas : The Methanol Economy*; Wiley-VCH, 2009.

(2) Khan, M. S.; Park, J. H.; Chaniago, Y. D.; Lee, M. Energy Efficient Process Structure Design of LNG/NGL Recovery for Offshore FLNG Plant. *Energy Procedia* **2014**, *61*, 599–602.

(3) Olivos-Suarez, A. I.; Szécsényi, À.; Hensen, E. J. M.; Ruiz-Martinez, J.; Pidko, E. A.; Gascon, J. Strategies for the Direct Catalytic Valorization of Methane Using Heterogeneous Catalysis: Challenges and Opportunities. *ACS Catal.* **2016**, *6*, 2965–2981.

(4) Da Silva, M. J. Synthesis of Methanol from Methane: Challenges and Advances on the Multi-Step (Syngas) and One-Step Routes (DMTM). *Fuel Processing Technology*. 2016, pp 42–61.

(5) Rosenzweig, A. C.; Nordlund, P.; Takahara, P. M.; Frederick, C. A.; Lippard, S. J. Geometry of the Soluble Methane Monooxygenase Catalytic Diiron Center in Two Oxidation States. *Chem. Biol.* **1995**, *2*, 409–418.

(6) Banerjee, R.; Proshlyakov, Y.; Lipscomb, J. D.; Proshlyakov, D. A. Structure of the Key Species in the Enzymatic Oxidation of Methane to Methanol. *Nature* **2015**, *518*, 431–434.

(7) Panov, G. I.; Sobolev, V. I.; Kharitonov, A. S. The Role of Iron in N2O Decomposition on ZSM-5 Zeolite and Reactivity of the Surface Oxygen Formed. *J. Mol. Catal.* **1990**, *61*, 85–97.

(8) Snyder, B. E. R.; Bols, M. L.; Schoonheydt, R. A.; Sels, B. F.; Solomon, E. I. Iron and Copper Active Sites in Zeolites and Their Correlation to Metalloenzymes. *Chem. Rev.* **2018**, *118*, 2718–2768.

(9) Snyder, B. E. R.; Vanelderen, P.; Bols, M. L.; Hallaert, S. D.; Böttger, L. H.; Ungur, L.; Pierloot, K.; Schoonheydt, R. A.; Sels, B. F.; Solomon, E. I. The Active Site of Low-Temperature Methane Hydroxylation in Iron-Containing Zeolites. *Nature* **2016**, *536*, 317–321.

(10) Snyder, B. E. R.; Böttger, L. H.; Bols, M. L.; Yan, J. J.; Rhoda, H. M.; Jacobs, A. B.; Hu, M. Y.; Zhao, J.; Alp, E. E.; Hedman, B.; Hodgson, K. O.; Schoonheydt, R. A.; Sels, B. F.; Solomon, E. I. Structural Characterization of a Non-Heme Iron Active Site in Zeolites That Hydroxylates Methane. *Proc. Natl. Acad. Sci.* **2018**, *115*, 4565–4570.

(11) Hallaert, S. D.; Bols, M. L.; Vanelderen, P.; Schoonheydt, R. A.; Sels, B. F.; Pierloot, K. Identification of α-Fe in High-Silica Zeolites on the Basis of Ab Initio Electronic Structure Calculations. *Inorg. Chem.* **2017**, *56*, 10681–10690.

(12) Dusselier, M.; Davis, M. E. Small-Pore Zeolites: Synthesis and Catalysis. *Chem. Rev.* **2018**, *118*, 5265–5329.

(13) Schmidt, J. E.; Deimund, M. A.; Xie, D.; Davis, M. E. Synthesis of RTH-Type Zeolites Using a Diverse Library of Imidazolium Cations. *Chem. Mater.* **2015**, *27*, 3756–3762.

(14) Di Iorio, J. R.; Gounder, R. Controlling the Isolation and Pairing of Aluminum in Chabazite Zeolites Using Mixtures of Organic and Inorganic Structure-Directing Agents. *Chem. Mater.* **2016**, *28*, 2236–2247.

(15) Dědeček, J.; Sobalík, Z.; Wichterlová, B. Siting and Distribution of Framework Aluminium Atoms in Silicon-Rich Zeolites and Impact on Catalysis. *Catal. Rev.* **2012**, *54*, 135–223.

(16) Alayon, E. M.; Nachtegaal, M.; Ranocchiari, M.; van Bokhoven, J. A. Catalytic Conversion of Methane to Methanol over Cu–mordenite. *Chem. Commun.* **2012**, *48*, 404–406.

(17) Baerlocher, C.; McCusker, L. B. Database of Zeolite Structures http://www.iza-structure.org/databases/ (accessed Apr 25, 2017).

(18) Ahlrichs, R.; Bär, M.; Häser, M.; Horn, H.; Kölmel, C. Electronic Structure Calculations on Workstation Computers: The Program System Turbomole. *Chem. Phys. Lett.* **1989**, *162*, 165–169.

(19) Dirac, P. A. M. Quantum Mechanics of Many-Electron Systems. *Proc. R. Soc. A Math. Phys. Eng. Sci.* **1929**, *123*, 714–733.

(20) Slater, J. C. A Simplification of the Hartree-Fock Method. *Phys. Rev.* **1951**, *81*, 385–390.

(21) Vosko, S. H.; Wilk, L.; Nusair, M. Accurate Spin-Dependent Electron Liquid Correlation Energies for Local Spin Density Calculations: A Critical Analysis. *Can. J. Phys.* **1980**, *58*, 1200–1211.

(22) Becke. Density-Functional Exchange-Energy Approximation with Correct Asymptotic Behavior. *Phys. Rev. A, Gen. Phys.* **1988**, *38*, 3098–3100.

(23) Lee, C.; Yang, W.; Parr, R. G. Development of the Colle-Salvetti Correlation-Energy Formula into a Functional of the Electron Density. *Phys. Rev. B* **1988**, *37*, 785–789.

(24) Becke, A. D. Density-functional Thermochemistry. III. The Role of Exact Exchange. *J. Chem. Phys.* **1993**, *98*, 5648–5652.

(25) Weigend, F.; Furche, F.; Ahlrichs, R. Gaussian Basis Sets of Quadruple Zeta Valence Quality for Atoms H–Kr. *J. Chem. Phys.* **2003**, *119*, 12753–12762.

(26) Schäfer, A.; Huber, C.; Ahlrichs, R. Fully Optimized Contracted Gaussian Basis Sets of Triple Zeta Valence Quality for Atoms Li to Kr. *J. Chem. Phys.* **1994**, *100*, 5829–5835.

(27) Andersson, K.; Malmqvist, P.; Roos, B. O. Second-order Perturbation Theory with a Complete Active Space Self-consistent Field Reference Function. *J. Chem. Phys.* **1992**, *96*, 1218–1226.

(28) Aquilante, F.; Autschbach, J.; Carlson, R. K.; Chibotaru, L. F.; Delcey, M. G.; De Vico, L.; Fdez. Galván, I.; Ferré, N.; Frutos, L. M.; Gagliardi, L.; Garavelli, M.; Giussani, A.; Hoyer, C. E.; Li Manni, G.; Lischka, H.; Ma, D.; Malmqvist, P. Å.; Müller, T. Molcas 8: New Capabilities for Multiconfigurational Quantum Chemical Calculations across the Periodic Table. *J. Comput. Chem.* **2016**, *37*, 506–541.

(29) Roos, B. O.; Lindh, R.; Malmqvist, P.-A.; Veryazov, V.; Widmark, P.-O. New Relativistic ANO Basis Sets for Transition Metal Atoms. *J. Phys. Chem. A* **2005**, *109*, 6575–6579.

(30) Roos, B. O.; Lindh, R.; Malmqvist, P.-A.; Veryazov, V.; Widmark, P.-O. Main Group Atoms and Dimers Studied with a New Relativistic ANO Basis Set. *J. Phys. Chem. A* **2004**, *108*, 2851–2858.

(31) Reiher, M.; Wolf, A. Exact Decoupling of the Dirac Hamlltonian. II. The Generalized Douglas-Kroll-Hess Transformation up to Arbitrary Order. *J. Chem. Phys.* **2004**, *121*, 10945–10956.

(32) Pierloot, K. The CASPT2 Method in Inorganic Electronic Spectroscopy: From Ionic Transition Metal to Covalent Actinide Complexes*. *Mol. Phys.* **2003**, *101*, 2083–2094.

(33) Pierloot, K. Nondynamic Correlation and TM Coordination Compounds. In *Computational Organometallic Chemistry*; Cundari, T. R., Ed.; New York, 2001; pp 123–158.

(34) Pierloot, K. Transition Metals Compounds: Outstanding Challenges for Multiconfigurational Methods. *International Journal of Quantum Chemistry*. Wiley Subscription Services, Inc., A Wiley Company November 5, 2011, pp 3291–3301.

(35) Veryazov, V.; Malmqvist, P. Å.; Roos, B. O. How to Select Active Space for Multiconfigurational Quantum Chemistry? *Int. J. Quantum Chem.* **2011**, *111*, 3329–3338.

(36) Vancoillie, S.; Zhao, H.; Tran, V. T.; Hendrickx, M. F. A.; Pierloot, K. Multiconfigurational Second-Order Perturbation Theory Restricted Active Space (RASPT2) Studies on Mononuclear First-Row Transition-Metal Systems. *J. Chem. Theory Comput.* **2011**, *7*, 3961–3977.

(37) Ghigo, G.; Roos, B. O.; Malmqvist, P.-Å. A Modified Definition of the Zeroth-Order Hamiltonian in Multiconfigurational Perturbation Theory (CASPT2). *Chem. Phys. Lett.* **2004**, *396*, 142–149.

(38) Forsberg, N.; Malmqvist, P.-Å. Multiconfiguration Perturbation Theory with Imaginary Level Shift. *Chem. Phys. Lett.* **1997**, *274*, 196–204.

(39) Neese, F. Prediction and Interpretation of the 57Fe Isomer Shift in Mössbauer Spectra by Density Functional Theory. *Inorganica Chim. Acta* **2002**, *337*, 181–192.

(40) Tomkins, P.; Mansouri, A.; Bozbag, S. E.; Krumeich, F.; Park, M. B.; Alayon, E. M. C.; Ranocchiari, M.; van Bokhoven, J. A. Isothermal Cyclic Conversion of Methane into Methanol over Copper-Exchanged Zeolite at Low Temperature. *Angew. Chemie Int. Ed.* **2016**, *55*, 5467–5471.

(41) Kazansky, V. B.; Kustov, L. M.; Borovkov, V. Y. Near Infrared Diffuse Reflectance Study of High Silica Containing Zeolites. *Zeolites* **1983**, *3*, 77–81.

(42) Karge, H. G. Characterization by IR spectroscopy http://www.iza-online.org/synthesis/VS_2ndEd/IR_Spectroscopy.htm (accessed Nov 12, 2017).

(43) Beck, K.; Pfeifer, H.; Staudte, B. Assignment of Novel Bands Observed in the near Infrared Spectra of Shallow-Bed Treated HY and HZSM-5 Zeolites. *Microporous Mater.* **1993**, *2*, 1–6.

(44) Hanke, W.; Möller, K. Near-Infrared Study of the Dealumination and Water Desorption from Zeolites. *Zeolites* **1984**, *4*, 244–250.

(45) Di Iorio, J. R.; Nimlos, C. T.; Gounder, R. Introducing Catalytic Diversity into Single-Site Chabazite Zeolites of Fixed Composition via Synthetic Control of Active Site Proximity. *ACS Catal.* **2017**, *7*, 6663–6674.

(46) Oh, S. J.; Cook, D. C.; Townsend, H. E. Characterization of Iron Oxides Commonly Formed as Corrosion Products on Steel. *Hyperfine Interact.* **1998**, *112*, 59–66.

(47) Sherman, D. M.; Waite, D. T. Electronic Spectra of Fe3 + Oxides and Oxide Hydroxides in the near IR to near UV. *Am. Mineral.* **1985**, *70*, 1262–1269.

(48) Marusak, L. A.; Messier, R.; White, W. B. Optical Absorption Spectrum of Hematite, αFe2O3 near IR to UV. *J. Phys. Chem. Solids* **1980**, *41*, 981–984.

(49) Shin, J.; Ahn, N. H.; Camblor, M. A.; Cho, S. J.; Hong, S. B. Intraframework Migration of Tetrahedral Atoms in a Zeolite. *Angew. Chemie Int. Ed.* **2014**, *53*, 8949–8952.

(50) Hendrickx, M. F. A.; Mironov, V. S.; Chibotaru, L. F.; Ceulemans, A. Assignment of the Electronic Spectra of [Mo(CN)8]4- and [W(CN)8]4- by Ab Initio Calculations. *Inorg. Chem.* **2004**, *43*, 3142–3150.

(51) Hendrickx, M. F. A.; Clima, S.; Chibotaru, L. F.; Ceulemans, A. [Mo2(CN)11]:5- A Detailed Description of Ligand-Field Spectra and Magnetic Properties by First-Principles Calculations. *J. Phys. Chem. A* **2005**, *109*, 8857–8864.

(52) Oleksiak, M. D.; Muraoka, K.; Hsieh, M.-F.; Conato, M. T.; Shimojima, A.; Okubo, T.;

Chaikittisilp, W.; Rimer, J. D. Organic-Free Synthesis of a Highly Siliceous Faujasite Zeolite with Spatially Biased Q^4 (*N* Al) Si Speciation. *Angew. Chemie Int. Ed.* **2017**, *56*, 13366–13371.

(53) Basaldella, E. I.; Tara, J. C. Synthesis of LSX Zeolite in the Na/K System: Influence of the Na/K Ratio. *Zeolites* **1995**, *15*, 243–246.

(54) Díaz-Cabañas, M.-J.; Barrett, P. A. Synthesis and Structure of Pure SiO2 Chabazite: The SiO2 Polymorph with the Lowest Framework Density. *Chem. Commun.* **1998**, *0*, 1881–1882.

(55) Zhang, R.; Liu, N.; Lei, Z.; Chen, B. Selective Transformation of Various Nitrogen-Containing Exhaust Gases toward N2 over Zeolite Catalysts. *Chem. Rev.* **2016**, *116*, 3658–3721.

(56) Martín, N.; Vennestrøm, P. N. R.; Thøgersen, J. R.; Moliner, M.; Corma, A. Fe-Containing Zeolites for NH3-SCR of NOx: Effect of Structure, Synthesis Procedure, and Chemical Composition on Catalytic Performance and Stability. *Chem. - A Eur. J.* **2017**, *23*, 13404–1341.

(57) Gao, F.; Zheng, Y.; Kukkadapu, R. K.; Wang, Y.; Walter, E. D.; Schwenzer, B.; Szanyi, J.; Peden, C. H. F. Iron Loading Effects in Fe/SSZ-13 NH_3 -SCR Catalysts: Nature of the Fe Ions and Structure–Function Relationships. *ACS Catal.* **2016**, *6*, 2939–2954.

(58) Xin, Y.; Li, Q.; Zhang, Z. Zeolitic Materials for DeNOx Selective Catalytic Reduction. *ChemCatChem* **2018**, *10*, 29–41.

(59) Brandenberger, S.; Kröcher, O.; Tissler, A.; Althoff, R. The State of the Art in Selective Catalytic Reduction of NO_x by Ammonia Using Metal-Exchanged Zeolite Catalysts. *Catal. Rev.* **2008**, *50*, 492–531.

TOC FIGURE

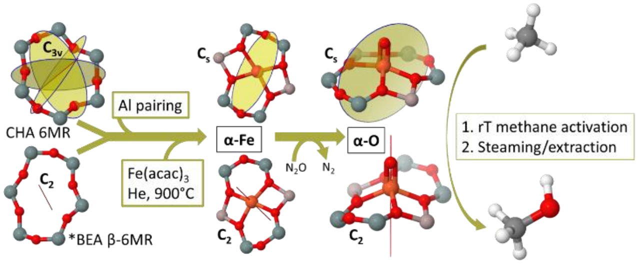
CHA 6MR
Al pairing
Fe(acac)$_3$
He, 900°C
*BEA β-6MR
α-Fe
N$_2$O
N$_2$
α-O
1. rT methane activation
2. Steaming/extraction